# Effect of delayed inhibitor supply on AA2024-T3 intermetallic activity
## A local in situ analysis with reflected microscopy

Mopon, Marlon; Mol, Arjan; Garcia, Santiago J.

**DOI**
10.1016/j.corsci.2024.111910

**Publication date**
2024

**Document Version**
Final published version

**Published in**
Corrosion Science

**Citation (APA)**
Mopon, M., Mol, A., & Garcia, S. J. (2024). Effect of delayed inhibitor supply on AA2024-T3 intermetallic activity: A local in situ analysis with reflected microscopy. *Corrosion Science*, *230*, Article 111910. https://doi.org/10.1016/j.corsci.2024.111910

Corrosion Science 230 (2024) 111910

Contents lists available at ScienceDirect

Corrosion Science

journal homepage: www.elsevier.com/locate/corsci

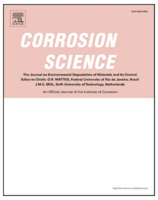

# Effect of delayed inhibitor supply on AA2024-T3 intermetallic activity: A local in situ analysis with reflected microscopy

Marlon Mopon Jr [a,b,*], Arjan Mol [c], Santiago J. Garcia [a,*]

[a] *Aerospace Structures and Materials Department, Delft University of Technology, Delft, the Netherlands*
[b] *Department of Chemical Engineering, University of the Philippines Diliman, Quezon City, Philippines*
[c] *Department of Material Science and Engineering, Delft University of Technology, Delft, the Netherlands*

## ARTICLE INFO

*Keywords:*
Corrosion inhibition
Metallographic microscopy
Inhibitor deposition kinetics
Difference imaging

## ABSTRACT

Understanding how late an inhibitor can be released once corrosion initiated without compromising corrosion protection may help in developing more efficient anticorrosion coatings. We explored this idea through time-controlled $Ce(NO_3)_3$ availability to AA2024-T3 immersed in 0.05 M NaCl. $Ce(NO_3)_3$ was supplied at 0, 30, 60, and 180 s from the start of immersion to get a concentration of 0.001 M. Detailed visualization of surface changes at the intermetallic particle level was obtained using in-situ reflected microscopy. SEM-EDX and confocal laser microscopy confirmed the extent of intermetallic degradation and local inhibitor deposition corresponding to operando changes. When the inhibitor is supplied within 60 s of immersion, the surface changes slowdown earlier and are visually less extensive than in uninhibited systems. Furthermore, our results highlight the potential of reflected microscopy for local corrosion inhibition studies and underscore the importance of understanding the interaction between inhibitor release timing and corrosion protection.

## 1. Introduction

AA2024-T3 is widely used in the aerospace industry due to its excellent strength-to-weight ratio. However, intermetallic particles (IMPs) formed during thermomechanical processing make it susceptible to local corrosion [1–3]. Coatings are typically used to reduce this corrosion susceptibility by providing barrier protection against corrosive environments. However, the protection provided by coatings is passive and is typically lost when there is mechanical damage that exposes the underlying metal. More reliable protection can be achieved by incorporation of active corrosion inhibition strategies [4–6]. This is typically accomplished by adding corrosion inhibitors [7–10] in the coatings. When the coating is damaged, the inhibitors are released to interact with the exposed metal surface, thereby constraining the extent of local corrosion.

Local corrosion at AA2024-T3 IMPs begins with the dealloying of IMPs [11–13]. This is characterized by the removal of less noble elements (e.g., Mg, Al) and subsequent enrichment of more noble components (e.g., Cu). In a recent study by Olgiati et al. [14], in situ reflected optical microscopy with kinetic analysis of image changes revealed that the surface activity at the IMP surface consistent with dealloying initiated within the first two minutes of exposure to 0.05 M NaCl (i.e., 23 ± 11 s for S-phase, 86 ± 12 s for AlCuFeMn, 79 ± 18 s for $(Al,Cu)_x(Fe,Mn)_ySi$). After a transition time (i.e., 68 ± 23 s for S-phase, 195 ± 48 s for AlCuFeMn, 224 ± 142 s for $(Al,Cu)_x(Fe,Mn)_ySi$), surface activity eventually develops at the adjacent matrix of the IMPs. This activity is attributed to Al dissolution (i.e., trenching) driven by galvanic coupling with the ennobled IMP. Given the rapid initiation of these local corrosion processes, it is crucial to have corrosion inhibitors readily available to minimize the extent of local corrosion. This has led to the development of active corrosion protection strategies that emphasize fast release [15–18] ideally followed by sustained supply of the inhibitor [19,20]. However, fast release and sustained supply are two competing aspects of inhibitor release since prioritising the former may affect the latter, which can then compromise the long-term reliability of the corrosion protection system [21].

Numerous strategies have been explored to prevent early inhibitor depletion in active corrosion protection systems. One effective approach involves using carriers with higher local inhibitor storage capacity [15,22,23] to enhance long-term availability of inhibitors. The higher inhibitor reserves, in principle, compensate for the initial fast release rates. Sacrificing some of these initial fast release capabilities is also a potential strategy to retain the inhibitors within the system for an extended period. This is a minimally studied approach given that slower

---

* Corresponding authors at: Aerospace Structures and Materials Department, Delft University of Technology, Delft, the Netherlands.
*E-mail addresses:* m.mopon@tudelft.nl (M. Mopon), j.m.c.mol@tudelft.nl (A. Mol), s.j.garciaespallargas@tudelft.nl (S.J. Garcia).

https://doi.org/10.1016/j.corsci.2024.111910
Received 28 October 2023; Received in revised form 5 January 2024; Accepted 8 February 2024

release rates would entail a certain degree of local corrosion. Nonetheless, this might be viable for precipitation-type inhibitors like cerium salts, which rely on local corrosion (i.e., dealloying) to deposit on the surface of IMPs [24–26].

Cerium deposition is influenced by the local alkalinity from the oxygen reduction reaction (ORR) occurring at the dealloying IMPs. The mechanistic interplay of dealloying-generated cathodic activity and cerium precipitation has been the subject of several studies. Li et al. [27] reported that depletion of Mg and Al due to dealloying in S-phase (i.e., $Al_2CuMg$) particles is needed for thick cerium deposits to form. On the other hand, Paussa et al. [28] found that fast magnesium dissolution during S-phase dealloying enables cathodic activity on nearby sites and accounts for the thick cerium deposits observed in S-phases. More recently, Kosari et al. [25] reported that the anodic and cathodic processes can occur simultaneously on IMPs from the onset of exposure, regardless of their composition. They identified dealloying as the primary factor in generating Cu-rich sites which facilitate cathodic reactions through nanogalvanic coupling with less noble regions of the IMP [11,12,25]. They emphasized the pivotal role of dealloying in determining the extent of cerium precipitation.

Based on the dealloying-driven mechanism of cerium precipitation coupled and the reported dealloying initiation times of AA2024-T3 IMPs, it can be argued that the cerium concentration does not necessarily need to be at a critical level at the very start of exposure to a corrosive solution for it to be protective. Thus, the initial inhibitor release from inhibition systems can be slowed down to a certain degree. This can lead to longer retention of Ce(III) within the system which allows for a more sustained release. A slower initial release effectively translates to delaying the availability of critical inhibitor concentrations to the surface of the IMPs. The delay in inhibitor availability, however, cannot be indefinite as this will result to significant local corrosion progression. Therefore, it seems necessary to determine a tolerable delay limit which can be used to extend inhibitor availability without compromising corrosion protection. We explored this idea in this work.

Here, an in situ reflected microscopy technique was used to analyse local surface changes when the availability of the inhibitor was intentionally delayed for a model system (i.e., electrolyte volume, electrolyte concentration, and inhibitor concentration are fixed). The microscopy technique previously enabled unprecedented visualization of intermetallic particle corrosion [14] and is thus promising for observing local inhibitor deposition and inhibitor layer growth. The technique allows surface observations at 1-second intervals of all IMPs within a field of view of approximately 800 ×600 microns (resolution: ~10 pixel $\mu m^{-2}$). This allows for the analysis of the concurrent behaviour of more IMPs, a limitation encountered in higher resolution in-situ methods like SKPFM [29,30] or EC-AFM [31,32]. $Ce(NO_3)_3$, further denoted as Ce(III), was used as the inhibitor for the system. Pre-immersion scanning electron microscopy with energy dispersive X-ray spectroscopy (SEM-EDX) was used to identify IMP composition which was then related to the surface changes observed. We quantified the extent and kinetics of these changes through a pixel subtraction-based image analysis protocol. The extent and kinetics were used to identify a tolerable delay limit specific to the model system conditions. Furthermore, we proposed mechanisms to elucidate why the inhibition behaviour varies at different Ce(III) supply times.

## 2. Experimental

### 2.1. Materials

Commercial grade bare AA2024-T3 (Kaiser Aluminium, rolled thickness = 2 mm) was used for the corrosion tests. Epoxy-embedded metal samples (EMS) with an exposed metal surface area of approximately 500 ×500 $\mu m^2$ were prepared from the metal sheets using a procedure described in earlier works [14,33]. Additional details on the preparation of the EMS are also provided in Supporting Information 1. A 0.05 M NaCl aqueous solution (>98% purity NaCl in "Millipore Elix 3 UV" treated water) was used as the corrosive solution while a 0.045 M $Ce(NO_3)_3$ + 0.05 M NaCl aqueous solution was used for adjusting the inhibitor concentration.

### 2.2. Experimental protocols

The experimental protocols used were adopted from earlier works [14,33]. The EMS surface was ground with SiC sandpaper from 320 to 4000 grit. They were then polished with 3 and 1 μm diamond paste. The location and spot composition of IMPs (i.e., around 100 – 200 particles per EMS) on the polished sample surface were determined using SEM-EDX (JEOL JSM-7500 F field emission scanning electron microscope coupled with energy dispersive X-ray spectroscopy). Back-scattered electron images were collected at a 15 kV accelerating voltage and a 10 μA emission current. The mapped EMS were quickly repolished (~10 s) with 1 μm diamond paste and washed in an ultrasonic bath containing ethanol before the immersion tests to remove contaminants from the SEM-EDX analysis. The EMS were placed in reflected microscopy setup (Fig. 1a) which involves a digital microscope (Dinolite AM7515MT4A, ~10 pixel $\mu m^{-2}$) operating in brightfield mode for in-situ acquisition of images of the surface during immersion [14]. The setup can also be used for electrochemical potential noise measurements during immersion, but this aspect of the experiment will be covered elsewhere. For the systems with non-delayed Ce(III) supply ($t_{supply} = 0$ s), a syringe was used to add 4.5 mL of 0.05 M NaCl + 0.001 M $Ce(NO_3)_3$ solution to the electrochemical cell. The electrolyte volume was dictated by the volume of our corrosion cell while the electrolyte solution was based on our previous work [14]. The time at which the EMS surface was fully exposed to the NaCl solution is t = 0. For the systems with delayed Ce(III) supply, a syringe was used to add 4.4 mL of the 0.05 M NaCl solution into the electrochemical cell. Corresponding volume of a 0.045 M $Ce(NO_3)_3$ solution was added using another syringe (27 gauge needle) at the delayed inhibitor supply times ($t_{supply} = 30, 60, 180$ s with respect to t = 0) to obtain a $Ce^{3+}$ concentration of 0.001 M. Additional details about our electrolyte injection protocol are provided in Supporting Information 2. The $t_{supply}$ values used were based on the $t_{onset}$ and transition times reported by Olgiati et al. for IMPs in AA2024-T3 exposed to 0.05 M NaCl [14]. At the $t_{supply}$ values selected, the IMP types identified are at different stages of dealloying and trenching: *(i)* at $t_{supply} = 0$ s (TS0), all the IMP types are inactive; *(ii)* at $t_{supply} = 30$ s (TS30), the S-phase IMPs are starting to dealloy; *(iii)* at $t_{supply} = 60$ s (TS60), S-phases have dealloyed considerably while the secondary particles (i.e., AlCuFeMn, $(Al,Cu)_x(Fe,Mn)_ySi)$) are just starting; *(iv)* at $t_{supply} = 180$ s (TS180), all IMP types are generally exhibiting advanced state of dealloying with signs of trenching. Immersion test in 0.05 M NaCl was also conducted to serve as control and to establish uninhibited behaviour of θ-phase. Duplicates of the delayed supply immersion tests were also implemented to confirm reproducibility (Supporting Information 3). After three hours of immersion, the EMS were removed from the corrosive environment, washed with deionized water, and dried in ambient conditions. Post-immersion analysis of the EMS was performed with a scanning laser confocal microscopy (SLCM) and SEM-EDX.

### 2.3. Image analysis

Surface changes were identified through a pixel-based analysis of the optical images based on our previously reported protocol [14]. Additional details about our protocol are provided in Supporting Information 4. In a first step, the processing involved conversion of the images to grayscale, recursive repositioning to align images, and subtraction of images (i.e., image @ 0 s – image @ *x* s) to identify the pixels that changed (i.e., darkened). These steps were implemented in ImageJ. The output of these steps is a grayscale image showing changed pixels for the entire EMS thereby providing the global activity map (GAM). A built-in

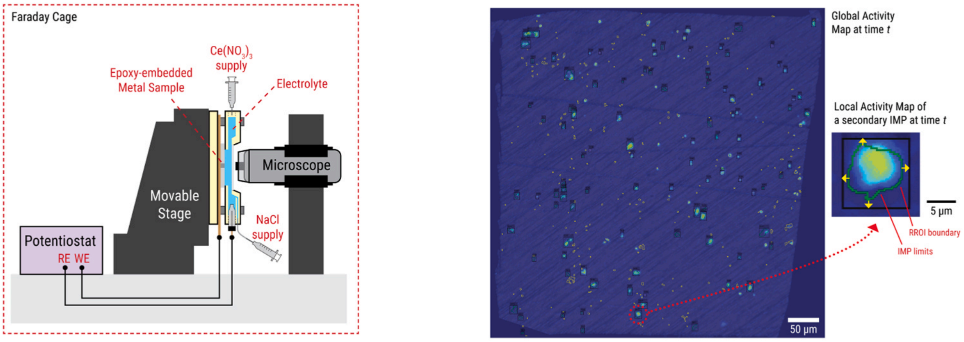

(a) (b)

**Fig. 1.** (a) in situ reflected microscopy setup (with electrochemical measurement capabilities) used to observe local surface changes during exposure to the electrolyte, and (b) a global activity map of an epoxy-embedded sample with IMP outlines and rectangular region of interest (RROI) boundaries used to establish the local activity maps. The global activity map is superimposed on an optical image (background) to highlight the position of the IMPs in the actual sample. The local activity map shows the degree of change of pixels at time t with respect to its initial condition (i.e., activity level) and the spatial distribution of the change.

ImageJ look-up table (i.e., Jet) was used to recolour the GAMs to enable easier visualisation of the magnitude of the changes (i.e., activity level).

The succeeding step involved local activity analysis of the IMPs with known composition using MatLab (MathWorks). IMP limits were set using the pre-immersion SEM-EDX data and superimposed on the GAMs using a method we reported previously [14]. Based on the EDX-derived composition, the IMPs were grouped into S-phases ($Al_2CuMg$), the θ-phases ($Al_2Cu$), and the secondary particles (AlCuFeMn or $(Al,Cu)_x(Fe,Mn)_ySi$)). It is emphasized that classification of the IMPs into compositional groups is based on the relative amounts of elements measured. Rectangular regions of interest (RROI) that surround the particles were set to isolate pixels specific to each intermetallic particle. The sides of the RROIs have a 4-pixel margin with respect to the left-, right-, top-, and bottom-most pixels of the particle border. The margin set was based on the affected area of selected particles after 600 s of exposure to 0.05 M NaCl. Ultimately, activity will likely extend beyond the RROI beyond 600 s but the changes that can be attributed to the intermetallic particles are presumed to be sufficiently captured. The RROIs are then superimposed on the GAM (Fig. 1b) to extract each IMP's local activity map (LAM). Around 100–200 LAMs were analysed per EMS.

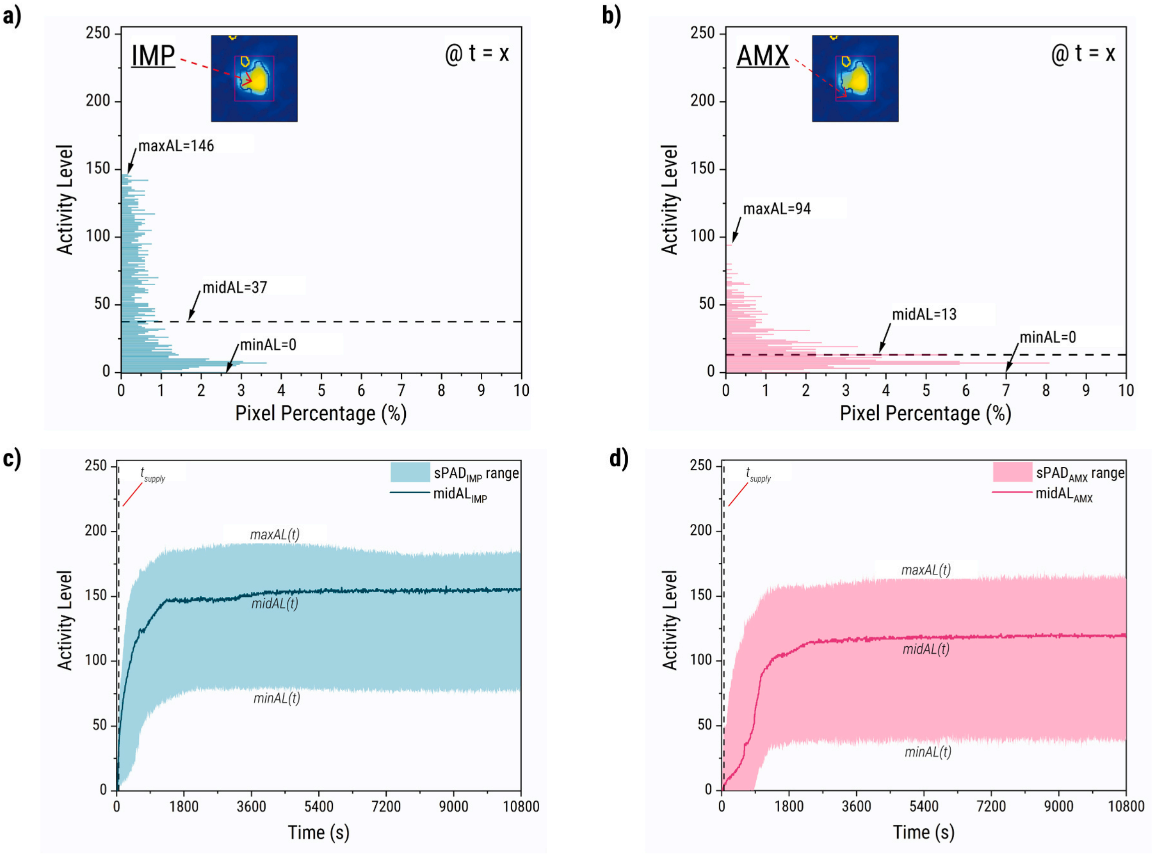

**Fig. 2.** Maximum, minimum, and median values are extracted from the **(a)** IMP, and **(b)** adjacent matrix pixel activity level distribution at time t. These were then used to build the simplified pixel activity distribution vs time plots for the **(c)** intermetallic particle pixels ($sPAD_{IMP}(t)$), and for the **(d)** adjacent matrix pixels ($sPAD_{AMX}(t)$). The resulting plots are used to assess the region involved with specific optical activity.

Local activity depicted in the LAMs are quantified in terms of the pixel activity level. This is equivalent to the pixel gray-level which ranges from 0 to 255, with 0 indicating no detected change with respect to the initial condition. The distribution of activity levels of the pixels in the LAMs and its kinetics is our primary means for quantitative analysis of the surface changes in this work. At a specific time *t*, the pixel activity level distribution of a given LAM can be represented in terms of a histogram generated using MatLab's built-in *imhist* function. The distribution can be extracted for both the IMP pixels (Fig. 2a) and the adjacent matrix pixels (Fig. 2b). The separate distributions are used to distinguish changes likely related to IMP processes (e.g., dealloying, inhibitor/oxide deposition) or to matrix processes (e.g., trenching, inhibitor/oxide deposition). For simpler analysis, the maximum (maxAL), minimum (minAL), and median activity levels (midAL) of the histograms are extracted. The midAL was favoured as the measure of central tendency because it is less sensitive to outliers. These three parameters are used to establish a simplified pixel activity level distribution for the IMP pixels ($sPAD_{IMP}$) and for the adjacent matrix pixels ($sPAD_{AMX}$). Measuring the sPAD at different times produces the time-series $sPAD_{IMP}(t)$ (Fig. 2b) and $sPAD_{AMX}(t)$ which enables analysis of the time-dependent trends of the surface changes. Compared to our previous method which focuses on measuring percentage of pixels that changed ($S_{changed}$ %) based on a lower bin threshold LTH, using the sPAD allows observation of changes even when *all* pixels in the LAM have activity levels greater the LTH (i.e., $S_{changed} = 100\%$). This is especially useful for assessing local inhibitor effect at the end of immersion.

It should be noted that analysis of the LAMs and the sPADs were focused on active IMPs (i.e., IMPs which exhibited detectable change). These IMPs were prioritised because we cannot be completely certain if inactivity in the presence of the inhibitor is due to the interaction with the inhibitor or due to the inherent stability of the IMPs during the immersion period investigated. Supporting Information 4provides additional details on how active IMPs were distinguished from inactive IMPs.

## 3. Results

### 3.1. Local behaviour of S-phase IMPs at different Ce(III) supply times

Fig. 3a shows LAMs of the representative S-phase IMP when Ce(III) is not present in the system. Distinct low-level activity (i.e., light blue pixels) at the IMP was observed within 35 s. This was followed by increase of the activity level of the IMP pixels and activation of adjacent matrix (AMX) pixels (i.e., appearance of light blue pixels in AMX). At 1800 s, the activity of the AMX pixels closest to the IMP boundary is higher than that of the IMP pixels. Further pixel activity increase was concentrated among these AMX pixels. Activation of new AMX pixels on the areas far from the IMP also progressed slowly from 1800 s as evident from minimal changes in the LAMs. The post-immersion SEM image shows that the IMP pixel activity is consistent with the IMP degradation (i.e., dealloying) while the high-level activity among the AMX pixels is consistent with trenching. Furthermore, the lower AMX activity on the pixels beyond the trench coincides with presence of scattered dark spots. Previous works attributed this to corrosion induced by redistributed Cu particles released by the degraded S-phase particle [11,24,34].

Fig. 3b shows there is a significant reduction in surface changes for the representative S-phase IMP at TS0 when compared to the uninhibited S-phase particle. Activity comparable to the initial changes of the uninhibited S-phase (i.e., activity at 35 s) were not observed until 1800 s. In spite of this activity during immersion, no signs of dealloying

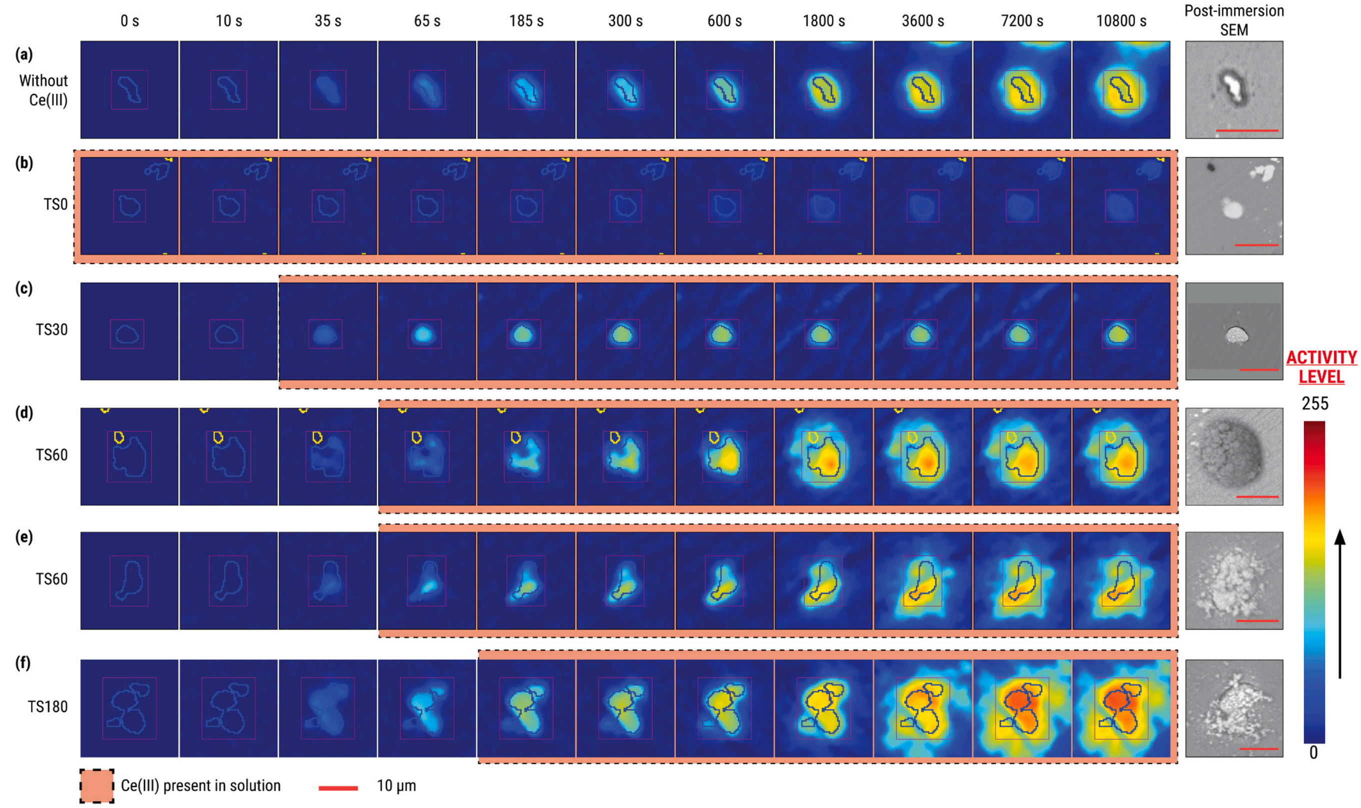

**Fig. 3.** Local activity maps (LAMs) of representative S-phase ($Al_2CuMg$) IMPs show evolution of the surface with time during exposure to **(a)** 0.05 M NaCl and with Ce(III) supplied at **(b)** 0, **(c)** 30, **(d)** 60 (visible corrosion product deposition), **(e)** 60 (visible Ce precipitation), and **(f)** 180 s from the start of immersion. The map colours represent the pixel activity level (i.e., change of the pixel gray-level with respect to its initial condition) at time t. The blue outline and the magenta rectangle overlaid on the map marks the IMP and RROI boundary, respectively. The LAMs highlight where the changes are happening in the context of the IMP and how extensive are the changes. The corresponding post-immersion back-scattered SEM images allude to the nature of the surface changes observed in the LAMs.

or trenching are visible in the post-immersion SEM image. However, spot composition approximated from the EDX spectra for the IMP surface indicated trace amounts of Ce (Atomic %: Ce ~ 0.3; Supporting Information 5 - Figure S11a). While this is not an accurate quantification, this suggests that the optical activity observed can be correlated to Ce deposition. Post-immersion SLCM analysis of another set of TS0 S-phase particles (Fig. 4a) with similar activity level (Fig. 4b) was used to estimate the scale of the corresponding Ce deposition. The SLCM images (Fig. 4c) of these particles show that there is indeed a height difference between the S-phase particles (point 1 and point 2) and the rest of the metal surface. In contrast, other particles within the region which have minimal optical activity (point 3) registered minimal height difference from the rest of the surface. The corresponding line profile through the S-phase IMPs (Fig. 4d) further indicates that the height difference is submicron (~ 0.1 µm). This coupled with the detected Ce in SEM/EDX point to submicron Ce deposition after three hours of immersion when the inhibitor is supplied at 0 s

Higher activity levels were generally observed for the TS30 S-phase IMP compared to the TS0 S-phase (Fig. 3c). The onset of low-level activity of the TS30 S-phase IMP is similar though to the uninhibited S-phase particle. After Ce(III) addition, there is a rapid increase of pixel activity which lasted until around 300 s at the IMP. This was accompanied by minimal activation of the AMX pixels. It should be noted that the slight reduction in activity between 7200 s and 10800 s is due to changes in the microscope lighting. The post-immersion back-scattered SEM image shows that the high IMP activity is associated with the formation of bright globular deposits which contain Ce (Atomic %: Ce ~ 4.8; Supporting Information 5 - Figure S11b). This further supports the correspondence between optically measurable activity and Ce(III) deposition and layer growth. Meanwhile, the lower AMX pixel activity is attributed to minimal changes on the adjacent matrix.

Matrix activity outside the RROI was also observed for the TS30 S-phase IMP. The exact nature of these changes is not yet known and warrants further investigation. Possible causes identified include deposition of corrosion products (e.g., aluminium (hydr)oxide), deposition of cerium, or nanometric changes in the oxide layer particularly on the scratched areas of the surface. This extra-RROI activity were also observed in the other TS30 particles, and even in the TS0, TS60, and TS180 systems. It was not as extensive though for TS0.

Fig. 3d and Fig. 3e show behaviour of two representative TS60 S-phase IMPs. The progression of their surface changes is generally comparable but the compositions of their deposited layer at the end of exposure have some interesting variation. Their initial activity is comparable with the uninhibited S-phase. After the addition of Ce(III), the changes became more similar to TS30. High activity spots were visible at the IMP surface of particles at around 65 s. These spots are likely preferential sites for Ce(III) deposition. The presence of these spots suggests compositional heterogeneity or differences in dealloying activity within the IMP. Unlike TS30, further deposition was observed for both particles, leading to increased AMX pixel involvement between 600 s and 1800 s. The changes appear to slow down after 1800 s which suggest minimal or no further deposition. Post-immersion back-scattered SEM image of the first TS60 S-phase (Fig. 3d) shows that the outline of thick dark deposited layer coincides with the active pixels in the LAMs. Based on EDX, the deposit contained Ce precipitates mixed with corrosion products (Atomic %: Ce ~ 0.8, Al ~ 27.5, O ~ 71.2; Supporting Information 5 - Figure S11c). Meanwhile, post-immersion back-scattered SEM image of the second TS60 S-phase (Fig. 3d) shows a bright deposit similar to the Ce-rich deposit observed for the TS30 S-phase. The higher amount of corrosion products on the deposited layer of the first TS60 S-phase is potentially due to a rupture of the initial Ce deposits. This could have enabled release and deposition of corrosion products on top of the Ce layer resulting in the dark colour observed.

S-phase behaviour at TS180 (Fig. 3e) is comparable to the behaviour in TS60. However, the TS180 particle exhibited continued surface changes for a longer duration (i.e., until around 7200 s) which points to sustained progression of the local processes that contribute to deposition. Post-immersion SEM shows narrow trenching around the IMP and irregular deposition on top of it. The deposit is comparable to the second TS60 S-phase (Fig. 3d). Based on EDX analysis of the IMP, the deposit contained Ce precipitates mixed with corrosion products (Atomic%: Ce ~ 8.0, Al ~ 11.2, O ~ 71.9; Supporting Information 5 - Figure S11d).

### 3.2. *Local behaviour of θ-phase IMPs at different Ce(III) supply time*

Fig. 5a shows that the onset of surface changes (i.e., appearance of light blue pixels on IMP) for uninhibited θ-phase particles is likely within the first minute of immersion, close to the onset of changes of uninhibited S-phase particles. A sample of 12 particles placed the mean activity onset for θ-phase particles at 43 ± 42 s. The high standard

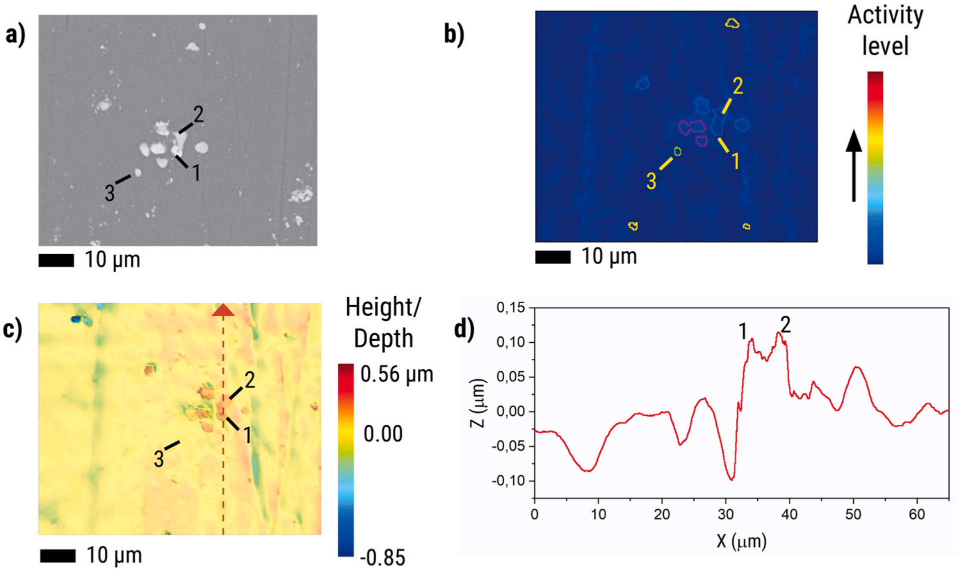

**Fig. 4.** **(a)** Pre-immersion SEM image of S-phase particles, and their **(b)** activity after three hours of exposure to 0.05 M NaCl and 0.001 M Ce(III) supplied at 0 s. The **(c)** SLCM images and corresponding **(d)** line profile for the particles indicate that low-level activity observed corresponds to submicron changes which we associate with Ce deposition.

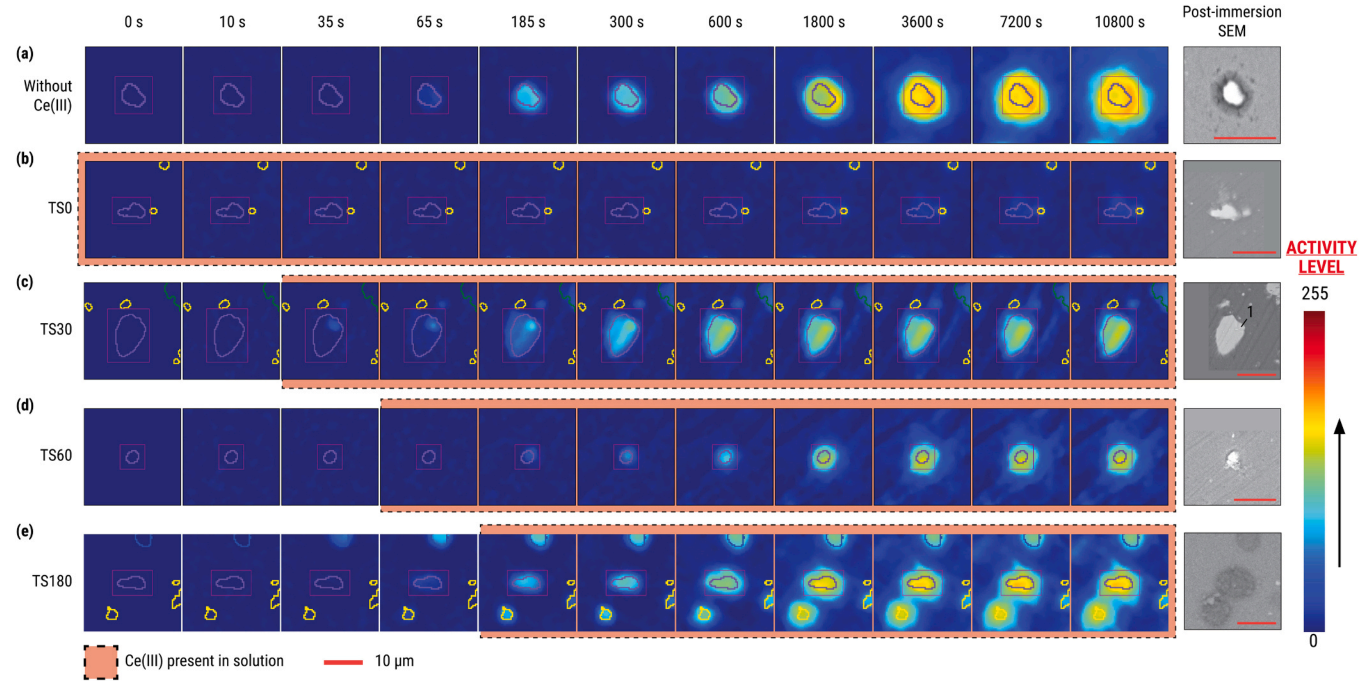

**Fig. 5.** Local activity maps (LAMs) of representative θ-phase ($Al_2Cu$) IMPs show evolution of the surface with time during exposure to **(a)** 0.05 M NaCl and with Ce (III) supplied at **(b)** 0, **(c)** 30, **(d)** 60, and **(e)** 180 s from the start of immersion. The map colours represent the pixel activity level (i.e., change of the pixel gray-level with respect to its initial condition) at time t. The purple outline and the magenta rectangle overlaid on the map marks the IMP and RROI boundary, respectively. The LAMs highlight where the changes are happening in the context of the IMP and how extensive are the changes. The corresponding post-immersion back-scattered SEM images allude to the nature of the surface changes observed in the LAMs.

deviation is attributed to the Mg content (0 – 2 at%) [35] of the particles as well as the potential heterogeneity within the particle [3]. Supporting Information 6 shows how the activity onset was quantified for the θ-phase IMPs. After the onset of activity, the subsequent increase of IMP and AMX pixel activity due to dealloying and trenching followed the same course as the uninhibited S-phase IMP. Matrix dissolution due to Cu redistribution is also observed as dark spots beyond the main trench.

Fig. 5b shows that the surface changes of the representative TS0 θ-phase IMP were also considerably reduced compared to the uninhibited θ-phase. Its behaviour during immersion is generally similar to the TS0 S-phase albeit with much lower activity levels. The optically detected changes are also attributed to submicron Ce deposition based on comparable activity and cerium detected on the IMP via EDX (Atomic %: Ce ~ 0.4; Supporting Information 5 - Figure S12a).

Distinct low-level activity for TS30 θ-phase (Fig. 5c) was observed at a spot on the IMP much earlier than the uninhibited θ-phase. The activation of this spot is comparable to that of the TS30 S-phase which suggests that it is also a preferential deposition site for Ce(III). This highly localized activity is attributed to higher concentration of less noble elements (e.g., Mg) on the region. This is typically encountered when an S-phase is embedded in a θ-phase IMP [36]. Activation of rest of the IMP and some of the AMX pixels due to further deposition was eventually observed. There were minimal changes though after 600 s. SEM-EDX analysis of the first active spot showed *visible* bright globular Ce-containing deposits (Atomic %: Ce ~ 2.3; Supporting Information 5 - Figure S12b). There were also some signs of dealloying in this region (dark spots in point 1 of Fig. 5c), but trenching was not apparent. Ce was also detected in the IMP region which activated much later but at a lower amount (Atomic %: Ce ~ 1.1; Supporting Information 5 - Figure S12c).

Fig. 5d shows that TS60 θ-phase IMP activity was not detectable until around 185 s, with similar mode to the region of the TS30 θ-phase IMP which activated much later. The surface changes of the IMP were also observed after the addition of Ce(III) to the solution indicating that it is deposition-related. The activity was concentrated at the IMP but increased activation of AMX pixels was also observed after 600 s. Surface changes were minimal after 3600 s. The post-immersion SEM image shows a narrow trench around the particle and more prominent deposition compared to the TS30 θ-phase IMP.

The initiation and progression of surface changes of the TS180 θ-phase (Fig. 5e) are generally similar to the TS60 θ-phase IMP. Activity associated with dealloying of the IMP surface was initially seen at around 65 s as expected for this type of IMP in 0.05 M NaCl solution. Once Ce(III) was added, simultaneous IMP pixel activity increase and AMX pixel activation associated with deposition was observed. Surface changes consistent with growth of the deposited layer continued until around 7200 s. The post-immersion back-scattered SEM image indeed shows a dark thick deposit covering the IMP similar to the first TS60 S-phase IMP. Meanwhile, EDX analysis shows that the deposit contains Ce precipitates mixed with corrosion products (Atomic %: Ce ~ 0.80, Al ~ 14.4, O ~ 83.98; Supporting Information 5 - Figure S12d).

### *3.3. Local behaviour of secondary IMPs at different Ce(III) supply time*

Fig. 6a shows that active secondary IMP (i.e., AlCuFeMn or (Al, Cu)$_x$(Fe,Mn)$_y$Si)) behaviour in uninhibited conditions is similar to the uninhibited S-phase and θ-phase IMPs. The dealloying onset on the IMP surface was observed between 65 and 185 s, consistent with the reported lower corrosion susceptibility of secondary IMPs [14]. The subsequent increase of IMP pixel activity as well as the activation of AMX pixels followed the same course as the other IMP types. The post-immersion SEM features of the particle are consistent with dealloying and trenching on the surrounding matrix. Matrix dissolution due to Cu redistribution is also observed as dark spots beyond the main trench. It is emphasized that not all secondary IMPs exhibited activity during exposure and the LAMs shown are representative only of the active secondary particles.

Fig. 6b shows that IMP pixel changes of the representative secondary IMP at TS0 were even more reduced than the corresponding S-phase and θ-phase IMPs. Comparison of the LAMs at 10 s and at 10800 s shows that

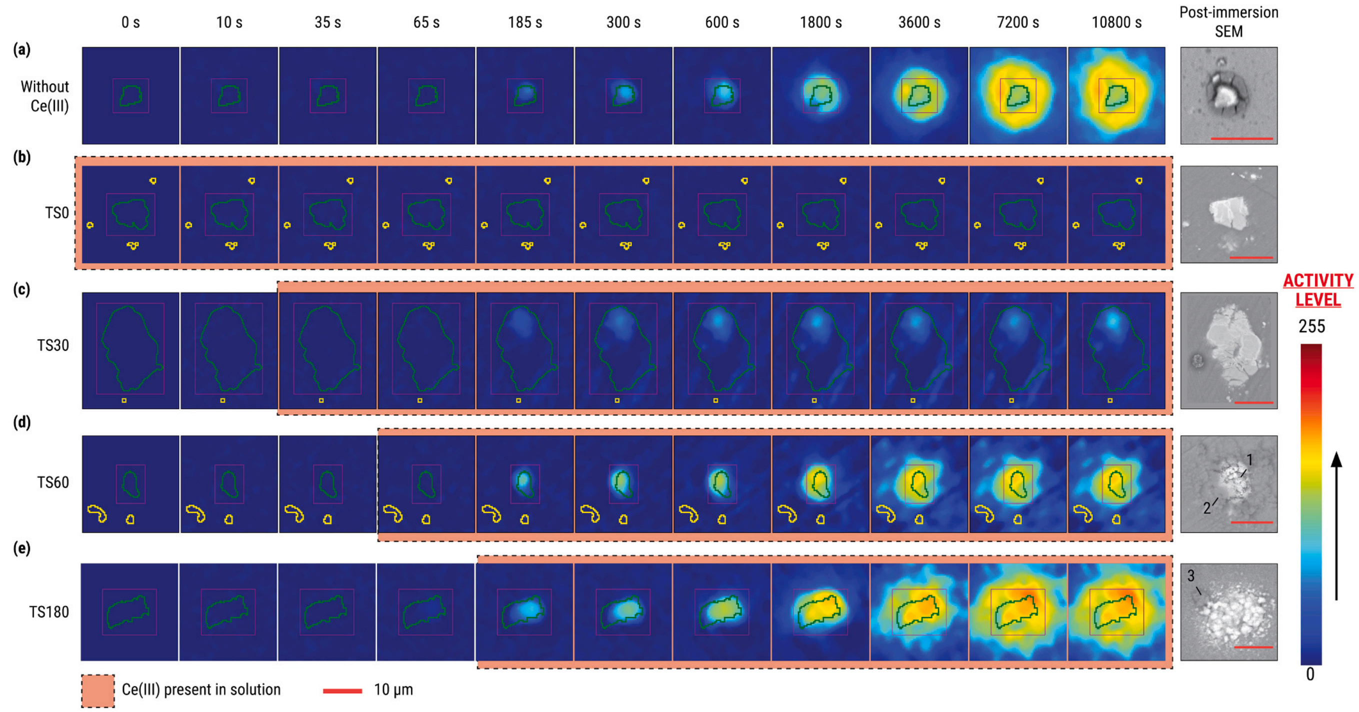

**Fig. 6.** Local activity maps (LAMs) of representative secondary (AlCuFeMn and $(Al,Cu)_x(Fe,Mn)_ySi$) IMPs show evolution of the surface with time during exposure to **(a)** 0.05 M NaCl and with Ce(III) supplied at **(b)** 0, **(c)** 30, **(d)** 60, and **(e)** 180 s from the start of immersion. The map colours represent the pixel activity level (i.e., change of the pixel gray-level with respect to its initial condition) at time t. The green outline and the magenta rectangle overlaid on the map marks the IMP and RROI boundary, respectively. The LAMs highlight where the changes are happening in the context of the IMP and how extensive are the changes. The corresponding post-immersion back-scattered SEM images allude to the nature of the surface changes observed in the LAMs.

there is slight activation of the IMP pixels. However, the activity is not as distinct from that of the surrounding matrix as with the other IMP compositions. The post-immersion SEM image shows no visible signs of dealloying or trenching, and Ce was not detected with EDX analysis (Supporting Information 5 - Figure S13a).

Partial activation of the IMP surface is observed for the representative secondary IMP at TS30 (Fig. 6c). Further immersion led to slight activity increase in this location but without further involvement of the other IMP pixels or the AMX pixels. No signs of significant dealloying or trenching is observed in the post-immersion SEM image, even on the active section of the IMP surface. However, trace amounts of Ce were also detected with EDX (Atomic %: Ce ~ 0.2; Supporting Information 5 - Figure S13b).

Activation of IMP pixels of the TS60 secondary IMP (Fig. 6d) was more pronounced than for TS0 and TS30. Similar to the other secondary IMPs, the spread of the activity to the entire IMP surface is slower relative to that for the S-phase and θ-phase particles. Continued immersion led to activity level increase of the pixels as well as further spread to the adjacent areas. The post-immersion SEM shows that the activity on the IMP surface (point 1 in Fig. 6d) likely corresponds to the deposition of Ce-containing precipitates (Atomic %: Ce ~ 11.8, Al ~ 15.2, O ~ 69.8; Supporting Information 5 - Figure S13c) while that on the AMX (point 2 in Fig. 6d) is consistent with the deposition of corrosion products (Atomic %: Ce ~ 0.5, Al ~ 71.0, O ~ 24.9; Supporting Information 5 - Figure S13d). The corrosion product deposits also appear to have originated from the edge of the area covered by cerium precipitates. This can indicate that the products might have been released from rupture sites of an initial precipitate layer formed on the IMP.

The progression of surface changes for the secondary IMP at TS180 (Fig. 6e) is generally similar to the TS60 particle. At 1800 s, almost all of the pixels in the RROI are active. After this time, extensive deposition led to widespread activation of the matrix pixels beyond the RROI. A large area covered by Ce-containing precipitates (Atomic %: Ce ~ 6.3, Al ~ 4.8, O ~ 87.6; Supporting Information 5 - Figure S13e) is apparent in the post-immersion SEM image. There are also visible corrosion product deposits (i.e., darker deposits) on the fringes of the Ce-rich area (point 3 in Fig. 6e).

### 3.4. *Activity levels and extent of inhibitor deposition*

The LAMs presented in the preceding sections illustrate the progression of surface changes at different Ce(III) supply times. Additionally, they demonstrate the correlation between pixel activity level measured during immersion and the extent of these surface changes. In systems supplied with Ce(III), the extent of surface changes directly relates to the amount of Ce precipitates formed and, consequently, the thickness of the deposits. This relationship becomes more evident when comparing the surface profiles of IMPs with varying levels of activity (Fig. 7a-c).

The low-level activity typically observed among TS0 particles is consistent with submicron changes, whereas medium- and high-level activity, observed with more delayed supply of Ce(III), are clearly related to micron-scale deposits. This correspondence is attributed to the scattering of incident light by the deposits [37]. As the deposits grow larger, they also scatter more light, resulting in a greater reduction in the intensity of light reflected back to the microscope. This then translates to darker pixels and higher LAM pixel activity level. Moreover, although the activity of the particles with significant deposition might seem similar to a typical corroded particle, the central positioning of the more active pixels can be used to distinguish deposition from advanced trenching (Fig. 7d). In particles with deposition, the activity is highest in the IMP and then drops as we move to the surrounding matrix. On the other hand, the uninhibited particles have medium to high activity on the IMP. The activity then increases further around the IMP boundary before eventually dropping further into the surrounding matrix. The high activity regions around the IMP boundary are due to extensive trenching observed in uninhibited particles.

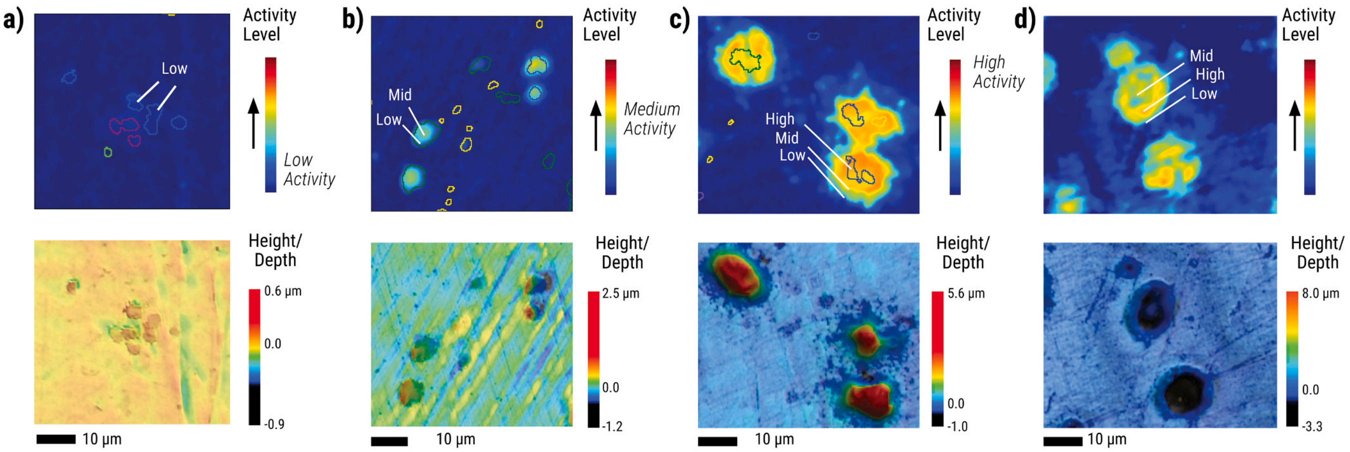

**Fig. 7.** Comparison of activity maps and SLCM images for representative IMPs show relative correspondence between thickness of the deposit and the observed pixel activity level for the IMPs supplied with Ce(III). **(a)** Low-level activity observed with TS0 IMPs appear to be nanometric while **(b)** medium (TS30 IMPs), and **(c)** high activity levels (TS180 IMPs) were consistent with increasing deposit thickness. The spatial distribution of the activity levels of the particles with deposits also appears to be different from **(d)** uninhibited particles.

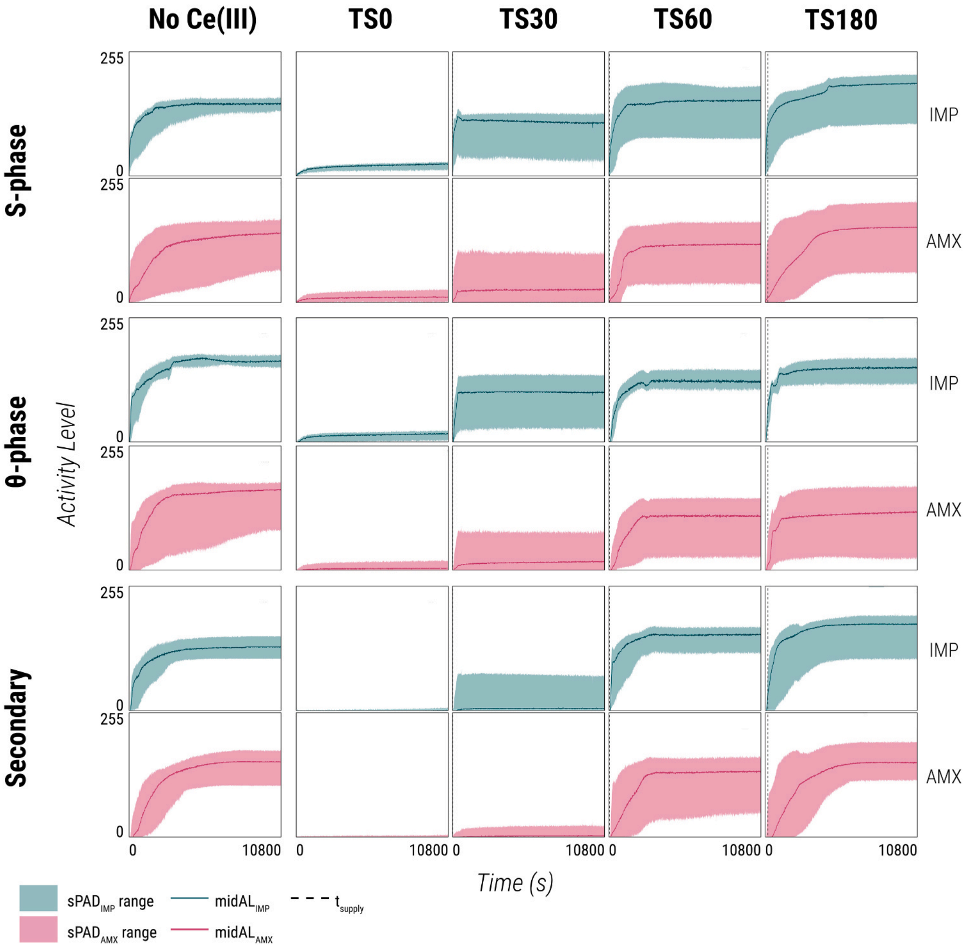

**Fig. 8.** Simplified pixel activity distribution (sPAD) plots of representative S-phase (Fig. 3a-d,f), θ-phase (Fig. 5), and secondary (Fig. 6) IMPs in the absence of Ce(III) and at different Ce(III) $t_{supply}$. The plots provide a clear picture of the period of rapid surface changes (fast period) and the period during which the surface changes slow down significantly (slow period). Activity level of the IMP and AMX pixels were separated to determine which location is more active during the immersion.

## 4. Discussion

### 4.1. Quantifying optical changes with simplified pixel activity distribution (sPAD) plots

A set of $sPAD_{IMP}(t)$ and $sPAD_{AMX}(t)$ plots were generated and compiled in Fig. 8 for the IMPs in Fig. 3(a-d,f), Fig. 5, and Fig. 6 to enable efficient comparison of the extent of surface changes among different IMP compositions and Ce(III) $t_{supply}$. The easiest means of comparison is by looking at activity levels at the end of the immersion (i.e., 10800 s), particularly the $midAL_{IMP}$ and $midAL_{AMX}$ as these values reflect the extent of deposition particularly for the IMPs exposed to Ce(III).

Regardless of the IMP composition, both $midAL_{IMP,3\,h}$ and $midAL_{AMX,3\,h}$ exhibit a drastic drop between the uninhibited and TS0 scenarios. However, the $midAL_{IMP,3\,h}$ and $midAL_{AMX,3\,h}$ increase again when Ce(III) is added later in time. It is noted though that the $midAL_{AMX,3\,h}$ values remained close to zero for both TS0 and TS30 for majority of the IMPs. This corresponds to the limited activation of adjacent matrix pixels observed in the corresponding LAMs. At TS60 and TS180, both $midAL_{IMP,3\,h}$ and $midAL_{AMX,3\,h}$ were already comparable to their uninhibited counterparts. This poses a challenge on optically differentiating trenching around IMPs from deposition on IMPs for these $t_{supply}$ values. Nonetheless, the values of $midAL_{IMP,3\,h}$ and $midAL_{AMX,3\,h}$ relative to each other appear to be useful in identifying which is the condition at hand. For trenching typically observed with uninhibited IMPs, $midAL_{AMX,3\,h}$ is comparable if not greater than the corresponding $midAL_{IMP,3\,h}$. On the other hand, widespread deposition on IMPs supplied with Ce(III) typically involve $midAL_{IMP,3\,h}$ values generally greater than the corresponding $midAL_{AMX,3\,h}$ values.

Fig. 9 shows $midAL_{IMP,3\,h}$ and $midAL_{AMX,3\,h}$ statistics for the active IMPs sampled at different inhibitor supply times. The relationship of the medians of the two parameters with $t_{supply}$ reflects the observations from the representative IMPs. It can also be observed that the increase from TS0 to TS30 is much higher for the $midAL_{IMP,3\,h}$ than the $midAL_{AMX,3\,h}$. This is because the initial period of uninhibited dealloying and subsequent inhibitor deposition for the TS30 particles mainly affect the IMP surface. Composition-dependent behaviour is also more easily observed from the median $midAL_{IMP,3\,h}$ and $midAL_{AMX,3\,h}$. For TS30 and TS60, a hierarchy of the median midAL values (i.e., S-phase > θ-phase > secondary) is observed and is associated with differences in the extent of IMP dealloying at the time when the inhibitor was added which leads to differences in degree of Ce precipitation. The same hierarchy is not distinct for TS180 likely due to the more extensive deposition. Indeed, at this $t_{supply}$, median $midAL_{IMP,3\,h}$ for all IMP compositions are already higher than the median values of the uninhibited particles.

Besides quantifying the extent of surface changes, the sPAD plots also enable analysis of the time-dependence of the surface changes. Fig. 8 shows that for most of the IMPs, both $sPAD_{IMP}(t)$ and $sPAD_{AMX}(t)$ are characterized by an overall period of fast activity level increase (fast period) which eventually transitions to an overall period of slow increase (slow period). The fast and slow periods themselves are composed of transitions of varying rates. The exact phenomena causing these transitions are not yet known but we attribute them either to local variations in activity due to compositional heterogeneity of the IMP, or changes in the composition of morphology of the deposits due to combined effect of local corrosion and inhibitor deposition. The first is associated with transitions in the fast period while the latter is associated with transitions in the slow period. For analysis of inhibition though, the relationship between the overall periods is considered to be more relevant. The transition time from the active to the slow period ($t_{sp}$) can be used as a temporal indicator of the inhibitory effect of the Ce (III) at different $t_{supply}$ values. It gives information about when the slow period becomes more dominant. Visually, the $t_{sp}$ is located around the shoulder between the active (i.e., increasing) and the slow (i.e., flat) periods of the sPAD plots. It is emphasized that estimation of the $t_{sp}$ is only possible with IMPs that exhibit activity. The procedure for quantitative determination of $t_{sp}$ is presented in detail in Supporting Information 7.

From the representative sPAD plots (Fig. 8), it is clear that regardless of IMP composition, the $t_{sp}$ of the uninhibited particles is observed much later than those of the inhibited ones. Furthermore, among the IMPs supplied with Ce(III), TS30 particles also appear to have the earliest $t_{sp}$. These observations are more apparent when $t_{sp}$ statistics (Fig. 10) are compared. Unlike with the $midAL_{IMP,3\,h}$ and $midAL_{AMX,3\,h}$ values, the effect of composition on the median $t_{sp}$ values appears to be less pronounced although a hierarchy (i.e., S-phase < θ-phase < secondary) can be observed for most of the $t_{supply}$ values. Given the $t_{sp}$ is associated with the duration of active deposition, the observed hierarchy suggests that the S-phase particles are capable of forming *stable* deposits much faster. The minima of the $t_{sp}$ at TS30 also suggests that initial uninhibited dealloying can speed up the inhibitor layer formation but only up to a certain degree.

### 4.2. Using reflective microscopy to estimate the tolerable delay limit for Ce(III) supply

Given that the $midAL_{IMP,3\,h}$, $midAL_{AMX,3\,h}$, and $t_{sp}$ provide a general overview of the surface changes, it makes sense to use them for estimating the tolerable delay for the supply of Ce(III). The tolerable delay essentially represents the maximum time after the star of the corrosion at which the inhibitor can be supplied and still obtain effective corrosion protection. From an optics-based consideration, the uninhibited parameters can be used as basis for evaluating if the behaviour at a specific $t_{supply}$ is tolerable or not. In the case of the $midAL_{IMP,3\,h}$ and

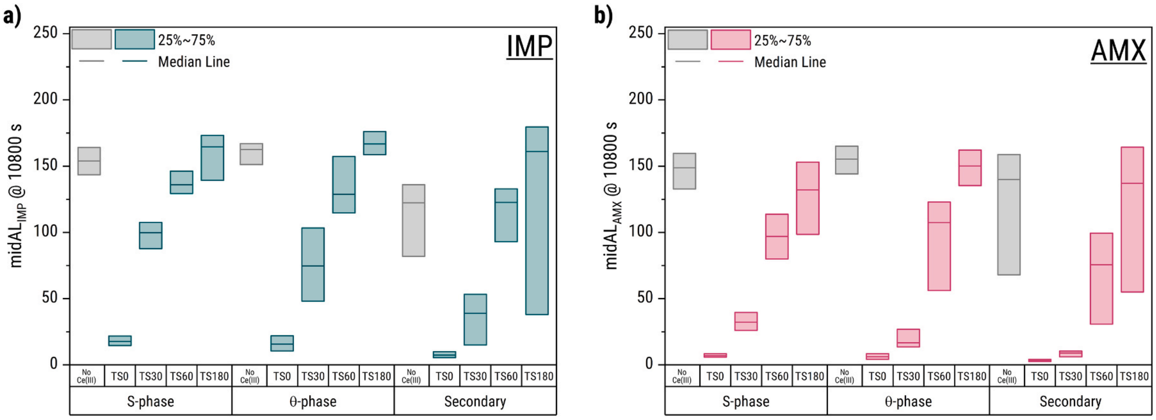

**Fig. 9.** Median (a) $midAL_{IMP,3\,h}$ and (b) $midAL_{AMX,3\,h}$ for the IMPs sampled show how the extent of surface changes varies with $t_{supply}$ and with IMP composition. In an ideal scenario, the $midAL_{IMP,3\,h}$ and $midAL_{AMX,3\,h}$ are minimal. Quantities corresponding to the plots are provided in Supporting Information 8.

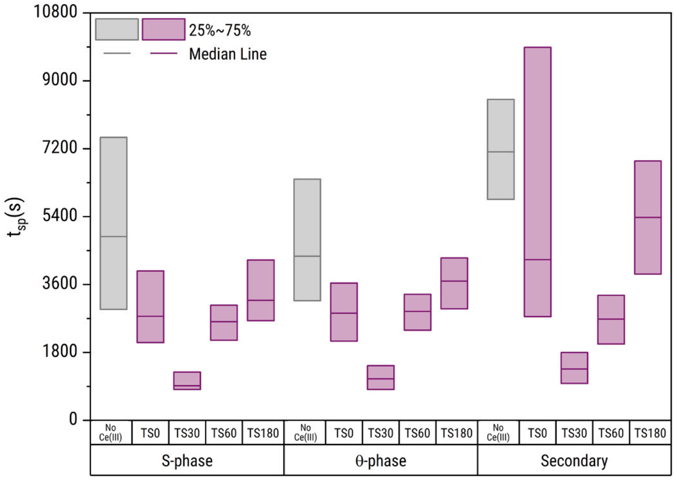

**Fig. 10.** Median $t_{sp}$ values measured for the IMPs analysed at different Ce(III) supply times show when the slow period starts to dominate. In an ideal scenario, the $t_{sp}$ is as low as possible (i.e., surface changes stabilise early) and the degree of change after the fast period is minimal. Quantities corresponding to the plot are provided in Supporting Information 8.

midAL$_{IAMX,3\ h}$, it is preferred that their values are less than those of a purely corroding surface. Indeed, the midAL values for the uninhibited and inhibited systems generally correspond to different surface features. They represent extent of dealloying and trenching for uninhibited IMPs and deposition for inhibited IMPs. Nonetheless, visual inspection is still one of the most accessible and intuitive means of evaluating corrosion [38–40]. As such, observing a tolerable delay limit that would not lead to confusion during maintenance inspections can be beneficial. As for the $t_{sp}$, it is ideal that the surface changes for the IMPs supplied with the inhibitor occur for a shorter period of time compared to the uninhibited IMPs (i.e., lower $t_{sp}$). This criterion provides us with a degree of certainty that the suppression of surface changes is due to the inhibitor presence and not just the inherent slowdown of local corrosion. Eqs. 1, 2, and 3 summarize the criteria for estimating the tolerable delay limit for a specific inhibition condition. The highest $t_{supply}$ which satisfies these criteria can be defined as the tolerable delay limit for the inhibitor at the specific experimental conditions.

$$\text{median}(\text{midAL}_{IMP,3h}) < \text{median}(\text{midAL}_{IMP,3h,uninhibited}) \tag{1}$$

$$\text{median}(\text{midAL}_{AMX,3h}) < \text{median}(\text{midAL}_{AMX,3h,uninhibited}) \tag{2}$$

$$\text{median}(t_{sp}) < \text{median}(t_{sp,uninhibited}) \tag{3}$$

.

Fig. 10 shows that the $t_{sp}$ criterion is satisfied for all of the $t_{supply}$ values tested. This implies that Ce(III) can still inhibit corrosion even when the supply is delayed. On the other hand, Fig. 9a shows that the midAL$_{IMP,3\ h}$ of the uninhibited IMPs are exceeded at TS180, for all IMP compositions. The same is evident for the median midAL$_{AMX,3\ h}$ (Fig. 9b) albeit the S-phase IMPs exhibited a slightly lower median than the uninhibited ones. Meanwhile, at TS60, the midAL values are high but they are considerable lower than the uninhibited IMPs for all compositions. In light of these observations, 60 s appears to be a sensible tolerable delay for the supply of Ce(III) to inhibit IMP local corrosion in AA2024-T3.

### 4.3. *Ce(III) precipitation at different supply time*

The midAL criterion used to estimate the tolerable delay limit is based on the high activity levels observed for delayed $t_{supply}$. These activity levels are attributed to the increase in the Ce(III) precipitation capacity of the IMPs. This is confirmed with post-immersion SEM and SLCM which showed more visible deposition compared to the TS0 IMPs. Furthermore, post-immersion EDX also highlighted increased presence of Ce at surface of the particles exposed to Ce(III) with delayed $t_{supply}$. The increase in the degree of precipitation is consistent with the dealloying-driven mechanism for inhibition with Ce(III). More delayed $t_{supply}$ corresponds to longer periods of uninhibited dealloying that leads to Cu enrichment. Enriched Cu sites increase the ORR rate on the IMP which provides the alkalinity required for Ce(III) to precipitate.

The interplay between local corrosion and Ce(III) precipitation at different $t_{supply}$, as well as the resulting local activity maps, are summarized in Fig. 11. Ce(III) presence right at the start of exposure (i.e., TS0) leads to highly localized precipitation which prevents dealloying from progressing significantly and, in turn, limits the extent of precipitation. It is hypothesized though that a sufficiently *thick* layer is still needed to effectively cut-off the ORR and the formation of this layer takes time. The $t_{sp}$ values for the TS0 particles reflects the time needed to form this layer. Moreover, the apparent hierarchy of $t_{sp}$ values among the different IMP types at TS0 also likely stems from varying capacity to support ORR and Ce(III) precipitation. The particles which dealloy easily (e.g., S-phase) can build thicker layers faster resulting to much earlier $t_{sp}$ than the others. The slowed down dealloying coupled with the limited Ce(III) precipitation leads to the observed low-level pixel activity concentrated at the IMP surface in the corresponding LAM.

The behaviour at TS30 can be considered as an accelerated version of TS0. The dealloying, particularly among S-phase and θ-phase IMPs, enabled faster precipitation of Ce(III) once it is added. However, since the dealloying is not yet extensive, the deposits that formed would have less defects and can slowdown surface changes much earlier (i.e., lower $t_{sp}$). The higher extent of Ce(III) precipitation translates to higher IMP pixel activity in the LAM. The inhibitor precipitation is also rapid and protective enough to control local corrosion progression which leads to limited activity in the adjacent matrix.

Higher degree of Ce precipitation observed in TS60 and TS180 does not necessarily correspond to more effective inhibition. Visibly increased fraction of corrosion products at the end of immersion for the TS60 and TS180 IMPs, in particular, indicates reduced protectiveness of the Ce deposits despite their increased thickness. When Ce(III) supply is more delayed, local corrosion processes can still proceed underneath the deposited layer. Transports of products from these processes such as metal ions or hydrogen [41,42] could potentially introduce defects in the Ce deposits. These defects provide paths for oxygen to reach the surface which then sustains ORR. As with TS0 and TS30, sufficient accumulation of cerium precipitates (and corrosion products) is also needed to control oxygen supply. This explains the higher $t_{sp}$ values observed with TS60 and TS180 IMPs as well as the more extensive deposition on the IMPs and their surrounding matrix by the time the surface changes slow down. In the LAMs, this is observed as high-level activity on both the IMP surface and the adjacent matrix. The presence of the inhibitor is still able to reduce the extent of local corrosion though leading to less extensive trenching relative to the uninhibited particles. This leads to pixels with highest activity levels still being situated within the boundaries of the IMPs.

## 5. Conclusion

An in situ reflected microscopy technique was used to analyse local surface changes when the availability of the inhibitor, $Ce(NO_3)_3$, was intentionally delayed to AA2024-T3. The technique combined with our image analysis protocol can be used to create GAMs (global activity maps), LAMs (local activity maps), and sPADs (simplified pixel activity level distribution). These are highly effective means of visualizing surface activation, local inhibitor deposition, and inhibitor layer growth at the intermetallic particle scale. GAMs and LAMs allow efficient analysis of the spatial dependence of the surface changes while the sPADs enable a simple method of visualizing the kinetics of said changes. Parameters extracted from the sPADs allowed comparison of the degree of changes

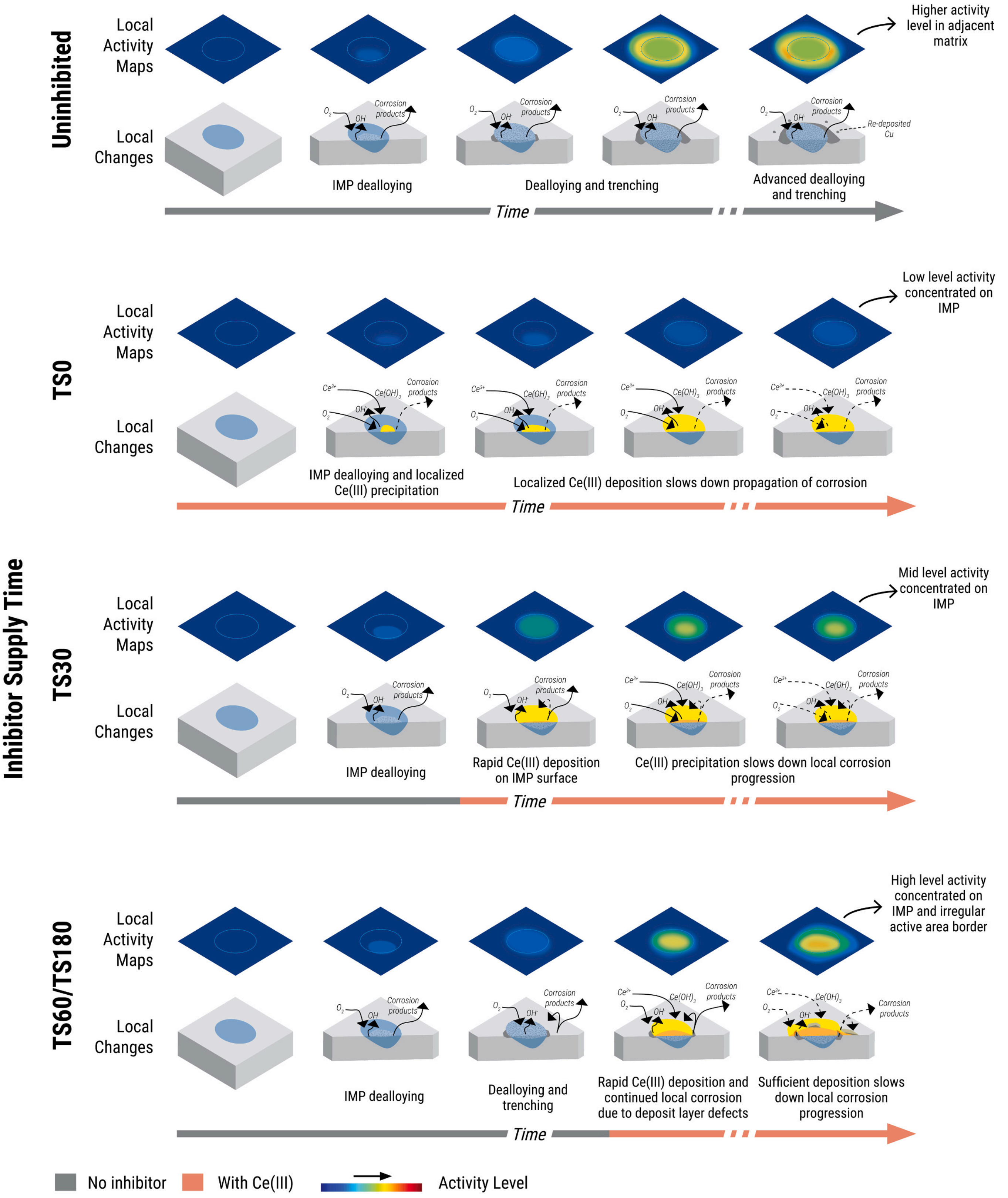

**Fig. 11.** Local changes in the absence of Ce(III) and when it is supplied at different times (i.e., 0, 30, 60, and 180 s from the start of exposure) and their corresponding local activity maps.

(i.e., $\text{midAL}_{\text{IMP},3\text{ h}}$, $\text{midAL}_{\text{IMP},3\text{ h}}$) and time at which the slow period dominates (i.e., $t_{sp}$) of IMPs at different inhibitor supply times. Based on these parameters and the experimental conditions used, when Ce(III) is supplied to the IMPs in our model system within 60 s of exposure, the surface changes associated with deposition slow down early, and the degree of these surface changes was less extensive than purely corroding particles. The tolerable delay of 60 s can potentially be applied as a basis for finetuning the design of anti-corrosion coatings in order to prolong inhibitor availability. It is emphasized though that its value is established from experiments where there is a burst release of Ce(III) at the specified $t_{supply}$ and no prior inhibitor presence. Furthermore, the results are also specific to the electrolyte and inhibitor concentrations used (i.e., 0.05 M NaCl, 0.001 M $Ce(NO_3)_3$). Assessing how this tolerable delay translates to more conventional release profiles can further enable better design and more effective screening of inhibitor delivery systems for active corrosion protection.

## CRediT authorship contribution statement

**Santiago J. Garcia:** Conceptualization, Funding acquisition, Methodology, Supervision, Visualization, Writing – original draft, Writing – review & editing. **Marlon Mopon Jr:** Investigation, Methodology, Visualization, Writing – original draft, Writing – review & editing. **Arjan Mol:** Conceptualization, Writing – original draft, Writing – review & editing.

## Declaration of Competing Interest

The authors declare that they have no known competing financial interests or personal relationships that could have appeared to influence the work reported in this paper.

## Data Availability

Data will be shared via a link to an online repository after the manuscript has been accepted (DOI: 10.4121/4e1a6d04-8076-4233-a672-24426251f0df).

## Acknowledgements

The author acknowledges the financial support by the DOST ERDT Program and the Faculty of Aerospace Engineering at TU Delft.

## Appendix A. Supporting information

Supplementary data associated with this article can be found in the online version at doi:10.1016/j.corsci.2024.111910.

## References

[1] L. Paussa, F. Andreatta, D. De Felicis, E. Bemporad, L. Fedrizzi, Investigation of AA2024-T3 surfaces modified by cerium compounds: a localized approach, Corros. Sci. 78 (2014) 215–222, https://doi.org/10.1016/J.CORSCI.2013.10.001.

[2] F.F. Chen, I. Cole, A.E. Hughes, A.M. Glenn, E. Sapper, J. Osborne, Microstructure characterisation and reconstruction of intermetallic particles, Mater. Corros. 65 (2014) 664–669, https://doi.org/10.1002/MACO.201307345.

[3] A.E. Hughes, R. Parvizi, M. Forsyth, Microstructure and corrosion of AA2024, Corros. Rev. 33 (2015) 1–30, https://doi.org/10.1515/corrrev-2014-0039.

[4] F.; Peltier, D. Thierry, D. Modestov, F. Peltier, D. Thierry, Review of Cr-Free Coatings for the Corrosion Protection of Aluminum Aerospace Alloys, Coatings 2022, Vol. 12, Page 518. 12 (2022) 518. https://doi.org/10.3390/COATINGS12040518.

[5] M.L. Zheludkevich, J. Tedim, M.G.S. Ferreira, Smart" coatings for active corrosion protection based on multi-functional micro and nanocontainers, Electrochim. Acta 82 (2012) 314–323, https://doi.org/10.1016/J.ELECTACTA.2012.04.095.

[6] I.S. Cole, Smart coatings for corrosion protection: an overview, Handb. Smart Coat. Mater. Prot. (2014) 29–55, https://doi.org/10.1533/9780857096883.1.29.

[7] T.G. Harvey, S.G. Hardin, A.E. Hughes, T.H. Muster, P.A. White, T.A. Markley, P. A. Corrigan, J. Mardel, S.J. Garcia, J.M.C. Mol, A.M. Glenn, The effect of inhibitor structure on the corrosion of AA2024 and AA7075, Corros. Sci. 53 (2011) 2184–2190, https://doi.org/10.1016/j.corsci.2011.02.040.

[8] K. Xhanari, M. Finšgar, Organic corrosion inhibitors for aluminum and its alloys in chloride and alkaline solutions: A review, Arab. J. Chem. 12 (2019) 4646–4663, https://doi.org/10.1016/J.ARABJC.2016.08.009.

[9] M. Bethencourt, F.J. Botana, J.J. Calvino, M. Marcos, M.A. Rodríguez-Chacón, Lanthanide compounds as environmentally-friendly corrosion inhibitors of aluminium alloys: a review, Corros. Sci. 40 (1998) 1803–1819, https://doi.org/10.1016/S0010-938X(98)00077-8.

[10] T.H. Muster, H. Sullivan, D. Lau, D.L.J. Alexander, N. Sherman, S.J. Garcia, T. G. Harvey, T.A. Markley, A.E. Hughes, P.A. Corrigan, A.M. Glenn, P.A. White, S. G. Hardin, J. Mardel, J.M.C. Mol, A combinatorial matrix of rare earth chloride mixtures as corrosion inhibitors of AA2024-T3: optimisation using potentiodynamic polarisation and EIS, Electrochim. Acta 67 (2012) 95–103, https://doi.org/10.1016/J.ELECTACTA.2012.02.004.

[11] A. Kosari, H. Zandbergen, F. Tichelaar, P. Visser, P. Taheri, H. Terryn, J.M.C. Mol, In-situ nanoscopic observations of dealloying-driven local corrosion from surface initiation to in-depth propagation, Corros. Sci. 177 (2020), https://doi.org/10.1016/J.CORSCI.2020.108912.

[12] A. Kosari, F. Tichelaar, P. Visser, H. Zandbergen, H. Terryn, J.M.C. Mol, Dealloying-driven local corrosion by intermetallic constituent particles and dispersoids in aerospace aluminium alloys, Corros. Sci. 177 (2020) 108947, https://doi.org/10.1016/j.corsci.2020.108947.

[13] A. Boag, A.E. Hughes, A.M. Glenn, T.H. Muster, D. McCulloch, Corrosion of AA2024-T3 Part I: Localised corrosion of isolated IM particles, Corros. Sci. 53 (2011) 17–26, https://doi.org/10.1016/j.corsci.2010.09.009.

[14] M. Olgiati, P.J. Denissen, S.J. Garcia, When all intermetallics dealloy in AA2024-T3: quantifying early stage intermetallic corrosion kinetics under immersion, Corros. Sci. (2021) 109836, https://doi.org/10.1016/j.corsci.2021.109836.

[15] P.J. Denissen, S.J. Garcia, Cerium-loaded algae exoskeletons for active corrosion protection of coated AA2024-T3, Corros. Sci. 128 (2017) 164–175, https://doi.org/10.1016/j.corsci.2017.09.019.

[16] Z. Li, Y. Shen, Y. Li, F. Zheng, L. Liu, Doping effects of cerium ion on structure and electrochemical properties of polyaniline, Polym. Int. 67 (2018) 121–126, https://doi.org/10.1002/PI.5487.

[17] L.R.L. Santos, C.E.B. Marino, I.C. Riegel-Vidotti, Silica/chitosan hybrid particles for smart release of the corrosion inhibitor benzotriazole, Eur. Polym. J. 115 (2019) 86–98, https://doi.org/10.1016/J.EURPOLYMJ.2019.03.008.

[18] P.J. Denissen, A.M. Homborg, S.J. Garcia, Requirements for corrosion inhibitor release from damaged primers for stable protection: a simulation and experimental approach using cerium loaded carriers, Surf. Coat. Technol. 430 (2022) 127966, https://doi.org/10.1016/J.SURFCOAT.2021.127966.

[19] E.L. Ferrer, A.P. Rollon, H.D. Mendoza, U. Lafont, S.J. Garcia, Double-doped zeolites for corrosion protection of aluminium alloys, Microporous Mesoporous Mater. 188 (2014) 8–15, https://doi.org/10.1016/j.micromeso.2014.01.004.

[20] P.J. Denissen, V. Shkirskiy, P. Volovitch, S.J. Garcia, Corrosion inhibition at scribed locations in coated AA2024-T3 by cerium- and DMTD-loaded natural silica microparticles under continuous immersion and wet/dry cyclic exposure, ACS Appl. Mater. Interfaces 12 (2020) 23417–23431, https://doi.org/10.1021/ACSAMI.0C03368/ASSET/IMAGES/LARGE/AM0C03368_0003.JPEG.

[21] C. Li, X. Guo, G.S. Frankel, Corrosion inhibition of AA2024-T3 by a coating containing dual-pH sensitive, corrosion inhibitor loaded microspheres, Corros. Sci. 192 (2021) 109835, https://doi.org/10.1016/J.CORSCI.2021.109835.

[22] D. Snihirova, S.V. Lamaka, M.M. Cardoso, J.A.D. Condeço, H.E.C.S. Ferreira, M. De Fatima Montemor, pH-sensitive polymeric particles with increased inhibitor-loading capacity as smart additives for corrosion protective coatings for AA2024, Electrochim. Acta 145 (2014) 123–131, https://doi.org/10.1016/J.ELECTACTA.2014.09.009.

[23] D. Snihirova, S.V. Lamaka, M. Taryba, A.N. Salak, S. Kallip, M.L. Zheludkevich, M. G.S. Ferreira, M.F. Montemor, Hydroxyapatite microparticles as feedback-active reservoirs of corrosion inhibitors, ACS Appl. Mater. Interfaces 2 (2010) 3011–3022, https://doi.org/10.1021/AM1005942/SUPPL_FILE/AM1005942_SI_001.PDF.

[24] K.A. Yasakau, M.L. Zheludkevich, S.V. Lamaka, M.G.S. Ferreira, Mechanism of corrosion inhibition of AA2024 by rare-earth compounds, Compd., J. Phys. Chem. B 110 (2006) 5515–5528, https://doi.org/10.1021/JP0560664/ASSET/IMAGES/MEDIUM/JP0560664E00026.GIF.

[25] A. Kosari, M. Ahmadi, F. Tichelaar, P. Visser, Y. Gonzalez-Garcia, H. Zandbergen, H. Terryn, J.M.C. Mol, Editors' Choice—Dealloying-Driven Cerium Precipitation on Intermetallic Particles in Aerospace Aluminium Alloys, J. Electrochem. Soc. 168 (2021) 041505, https://doi.org/10.1149/1945-7111/abf50d.

[26] N.C. Rosero-Navarro, M. Curioni, R. Bingham, A. Durán, M. Aparicio, R.A. Cottis, G.E. Thompson, Electrochemical techniques for practical evaluation of corrosion inhibitor effectiveness. Performance of cerium nitrate as corrosion inhibitor for AA2024T3 alloy, Corros. Sci. 52 (2010) 3356–3366, https://doi.org/10.1016/J.CORSCI.2010.06.012.

[27] J. Li, B. Hurley, R. Buchheit, The effect of CeCl 3 as an inhibitor on the localized corrosion of AA2024-T3 as a function of temperature, J. Electrochem. Soc. 163 (2016) C845–C852, https://doi.org/10.1149/2.0561614jes.

[28] L. Paussa, F. Andreatta, N.C. Rosero Navarro, A. Durán, L. Fedrizzi, Study of the effect of cerium nitrate on AA2024-T3 by means of electrochemical micro-cell technique, Electrochim. Acta 70 (2012) 25–33, https://doi.org/10.1016/J.ELECTACTA.2012.02.099.

[29] L. Lacroix, L. Ressier, C. Blanc, G. Mankowski, Statistical study of the corrosion behavior of Al[sub 2]CuMg intermetallics in AA2024-T351 by SKPFM, J. Electrochem. Soc. 155 (2008) C8, https://doi.org/10.1149/1.2799089/XML.

[30] T. Hu, H. Shi, D. Hou, T. Wei, S. Fan, F. Liu, E.H. Han, A localized approach to study corrosion inhibition of intermetallic phases of AA 2024-T3 by cerium malate, Appl. Surf. Sci. 467–468 (2019) 1011–1032, https://doi.org/10.1016/J.APSUSC.2018.10.243.

[31] N. Li, C. Dong, C. Man, J. Yao, In situ electrochemical atomic force microscopy and auger electro spectroscopy study on the passive film structure of 2024-T3 aluminum alloy combined with a density functional theory calculation, Adv. Eng. Mater. 21 (2019) 1900386, https://doi.org/10.1002/ADEM.201900386.

[32] A. Kreta, M. Rodošek, L. Slemenik Perše, B. Orel, M. Gaberšček, A. Šurca Vuk, In situ electrochemical AFM, ex situ IR reflection–absorption and confocal Raman studies of corrosion processes of AA 2024-T3, Corros. Sci. 104 (2016) 290–309, https://doi.org/10.1016/J.CORSCI.2015.12.023.

[33] A.M. Homborg, M. Olgiati, P.J. Denissen, S.J. Garcia, An integral non-intrusive electrochemical and in-situ optical technique for the study of the effectiveness of corrosion inhibition, Electrochim. Acta 403 (2022) 139619, https://doi.org/10.1016/J.ELECTACTA.2021.139619.

[34] R.G. Buchheit, R.P. Grant, P.F. Hlava, B. Mckenzie, G.L. Zender, Local dissolution phenomena associated with S phase ( Al2CuMg) particles in aluminum alloy 2024-T3, J. Electrochem. Soc. 144 (1997) 2621–2628, https://doi.org/10.1149/1.1837874.

[35] A.E. Hughes, A.M. Glenn, N. Wilson, A. Moffatt, A.J. Morton, R.G. Buchheit, A consistent description of intermetallic particle composition: an analysis of ten batches of AA2024-T3, Surf. Interface Anal. 45 (2013) 1558–1563, https://doi.org/10.1002/SIA.5207.

[36] X. Zhang, T. Hashimoto, J. Lindsay, X. Zhou, Investigation of the de-alloying behaviour of θ-phase (Al2Cu) in AA2024-T351 aluminium alloy, Corros. Sci. 108 (2016) 85–93, https://doi.org/10.1016/J.CORSCI.2016.03.003.

[37] P.M.F. Forte, P.E.R. Felgueiras, F.P. Ferreira, M.A. Sousa, E.J. Nunes-Pereira, B.P. J. Bret, M.S. Belsley, Exploring combined dark and bright field illumination to improve the detection of defects on specular surfaces, Opt. Lasers Eng. 88 (2017) 120–128, https://doi.org/10.1016/J.OPTLASENG.2016.08.002.

[38] P.A. White, A.E. Hughes, S.A. Furman, N. Sherman, P.A. Corrigan, M.A. Glenn, D. Lau, S.G. Hardin, T.G. Harvey, J. Mardel, T.H. Muster, S.J. Garcia, C. Kwakernaak, J.M.C. Mol, High-throughput channel arrays for inhibitor testing: Proof of concept for AA2024-T3, Corros. Sci. 51 (2009) 2279–2290, https://doi.org/10.1016/J.CORSCI.2009.06.038.

[39] B. Brandoli, A.R. de Geus, J.R. Souza, G. Spadon, A. Soares, J.F. Rodrigues, J. Komorowski, S. Matwin, Aircraft fuselage corrosion detection using artificial intelligence, 4026. 21, Sensors 2021 Vol. 21 (2021) 4026, https://doi.org/10.3390/S21124026.

[40] S. Agnisarman, S. Lopes, K. Chalil Madathil, K. Piratla, A. Gramopadhye, A survey of automation-enabled human-in-the-loop systems for infrastructure visual inspection, Autom. Constr. 97 (2019) 52–76, https://doi.org/10.1016/J.AUTCON.2018.10.019.

[41] H. Ju, S. Liu, W. Zhang, Y. Yang, J. Duan, Investigation of pitting corrosion and hydrogen evolution of aluminum and AA2024 alloy by simultaneous electrochemical measurements and imaging, Electrochem. Commun. 132 (2021) 107135, https://doi.org/10.1016/J.ELECOM.2021.107135.

[42] C. Laurent, F. Scenini, T. Monetta, F. Bellucci, M. Curioni, The contribution of hydrogen evolution processes during corrosion of aluminium and aluminium alloys investigated by potentiodynamic polarisation coupled with real-time hydrogen measurement, Npj Mater. Degrad. 2017 11 1 (2017) 1–7, https://doi.org/10.1038/s41529-017-0011-4.